Nanoscale

PAPER

View Article Online
View Journal | View Issue



Cite this: *Nanoscale*, 2025, **17**, 24110

# Fuel-driven filamentous phage nanomotors

Xi Ding,[a] Shamima Zaman,[b] Emily P. Africa,[c] Bahman Anvari[b] and Elaine D. Haberer*[a,c]

Received 11th June 2025,
Accepted 28th September 2025

DOI: 10.1039/d5nr02501j

rsc.li/nanoscale

Virus-based nanocarriers have shown great potential for noninvasive delivery of drugs, diagnostics, and imaging agents to hard-to-reach anatomical locations. Yet, they largely depend on diffusion for transport, often lacking the force to actively penetrate biological barriers, and navigation to guide therapeutic agents. In these studies, the M13 bacteriophage, a linearly shaped virus, was converted from passive nanocarrier to actively propelled, fuel-driven nanomotor. Using the distinctive low symmetry of its capsid, a single Pt nanoparticle was added to one end of the M13 virus to form a tadpole-like structure. The Pt/M13 head/tail nanomotors exhibited notably enhanced diffusion in the presence of hydrogen peroxide fuel, and significantly improved uptake by SVOK3 ovarian cancer cells *in vitro*. Given the successes of the M13 bacteriophage as a nanocarrier, the demonstration of this simple, but comparatively mobile M13-based nanomotor platform represents an important step in advancing the potential therapeutic efficacy of viral nanocarriers.



## 1. Introduction

The advent of nanoscale particles and structures has fueled the development of nanomedicine. Colloidal structures, commonly known as nanocarriers, have the potential for noninvasive delivery of drugs, diagnostics, and imaging agents to otherwise inaccessible regions of the body.[1] Given the breadth of environments and challenges presented by human physiology, a diverse nanocarrier tool set is necessary. A number of material candidates, both organic (*e.g.* liposomes, proteins) and inorganic (*e.g.* metallic- or oxide-based nanocrystals), are under investigation.[2] Increasingly, structures composed of natural, biocompatible substances have garnered attention. Viruses or virus-based nanoparticles are one such example.[3,4] These multivalent, monodisperse bionanomaterials are whole bacteriophage, plant viruses, or repeating viral structural proteins that are noninfectious to humans. Their well-controlled surface chemistry contributes to easy functionalization, relatively straightforward cargo loading[4–6] and location specific targeting within the body. Moreover, because capsids range widely in size and shape, viral nanocarrier geometry can be selected to match precise therapeutic objectives.

In recent years, the filamentous M13 bacteriophage has drawn interest as a nanocarrier.[7] It has proven useful for a variety of potential nanomedicine applications including noninvasive imaging and surgical guidance for tumor extraction,[8,9] targeted delivery of cancer drugs and photodynamic therapy,[10–14] and treatment of bacterial infections.[15–17] The M13 wild type is a semi-flexible fiber 880 nm in length and 6.5 nm in diameter. Its length can be tuned genetically for optimal nanocarrier performance.[13,18] Compared to more isotropic geometries, its small diameter and linear shape facilitate delivery to hard-to-reach anatomical locations including those with highly restrictive pore sizes such as the brain.[19,20] Five structural proteins comprise its capsid. In addition to being easily functionalized, these viral coat proteins are extraordinarily adaptable. As demonstrated by its widespread use in combinatorial phage display, the M13 can be genetically engineered to accommodate an impressive range of surface moieties of various sizes and characters. Affinity fusions identified by biopanning are necessarily stable within its capsid and can be used directly within the viral nanocarrier without additional steps. The pIII, a minor coat protein, and the pVIII, a major coat protein, are used most regularly for combinatorial display. Five copies of the pIII cap the proximal end of the virus while approximately 2700 copies of the pVIII make up the wild type phage body. The multivalency of these two proteins is particularly advantageous for a nanocarrier platform, supporting increased affinity through avidity in addition to superior payload capacity. The pIII and pVIII can be separately modified chemically, genetically, or both. This facilitates a high degree of orthogonality, allowing convenient and independent control over targeting and loading tasks.[10,13,21] The overall structure of the M13 capsid is also highly stable. It can readily withstand

[a]*Department of Electrical and Computer Engineering, University of California, Riverside, CA, 92521, USA. E-mail: haberer@ucr.edu*
[b]*Department of Bioengineering, University of California, Riverside, CA, 92521, USA*
[c]*Materials Science and Engineering Program, University of California, Riverside, CA, 92521, USA*

the span of pHs and mechanical stresses present within the human body.[22,23] As a lysogenic bacteriophage, the M13 can also be inexpensively mass produced in a reactor, making wide spread medical use feasible.[24,25]

Despite many advantages, M13 nanonarriers are ultimately passive delivery vehicles. Like their inorganic counterparts, these bio-based nanoparticles rely primarily on diffusion for transport. Passive particles lack the force to actively penetrate biological barriers, and navigation to guide therapeutic agents precisely to their intended destination. Despite targeting ligands, their accumulation often continues to depend heavily on the enhanced permeation and retention effect, which can be inefficient, resulting in slow delivery and a considerable off-target distribution.[26] Nanomotors, nanoscale structures that convert energy from their surroundings into locomotion, have potential to overcome these limitations. These tiny robots are powered by catalytic reactions with chemical fuels or externally controlled fields. Fuel-driven propulsion is often achieved through structural or compositional asymmetry. Build-up of reaction products on one side of a Janus particle creates thrust, producing autonomous motion. While still emergent, nanomotors have made remarkable advances in nanomedicine.[27–37] From relatively simple Pt-capped mesoporous silica nanoparticles to more sophisticated icebreaker-inspired nanorods that incorporate both a means of propulsion and path-clearing digestion of the extracellular matrix, nanomotors have repeatedly demonstrated enhanced delivery by accelerating motion and breaking through barriers.[38,39] This superior mobility has yet to be fully exploited by viral nanocarriers. The marriage of viral nanocarrier specificity with nanomotor active propulsion has the potential to markedly improve therapeutic efficacy while diminishing adverse side effects caused by off-target toxicity. Thus far, viral nanomotors have been composed of icosahedral capsids sputter coated to form a Pt hemisphere for symmetry breaking and propulsion.[40] The aforementioned semi-flexible linear shape,[19,20] capacity for orthogonal functionalization,[10,13,21] and innately low structural symmetry of the M13 bacteriophage make it a promising candidate for viral nanomotor design and assembly.

Here, we report a simple M13-templated fuel-driven nanomotor for increased cellular internalization. As illustrated in Fig. 1, using the nonuniform distribution of cysteine residues within its filament-shaped capsid, a single Pt nanoparticle was attached to one end of a genetically modified cysteine-enriched M13 bacteriophage *via* metal–sulfur bonding, forming a tadpole-like geometry. The nanoparticle served as both a propulsion mechanism and a near infrared (NIR) photothermal agent. Trajectories of fluorescently tagged Pt/M13 nanomotors were recorded with confocal laser scanning microscopy (CLSM) in a range of $H_2O_2$ concentrations. Propulsion, triggered by the addition of fuel, was accelerated with increasing concentration. Compared to the M13 phage, Pt/M13 nanomotors exhibited notably enhanced diffusion. Their improved transport significantly boosted uptake by SVOK3 ovarian cancer cells *in vitro*. The laser-activated photothermal properties of the Pt/M13 nanomotors were also evaluated. Following nanomotor internalization, cell viability was adversely affected by 808 nm light. Given the successes of the M13 bacteriophage as a nanocarrier, the demonstration of this simple, but comparatively mobile M13-based nanomotor platform has the potential to dramatically enhance its therapeutic efficacy.

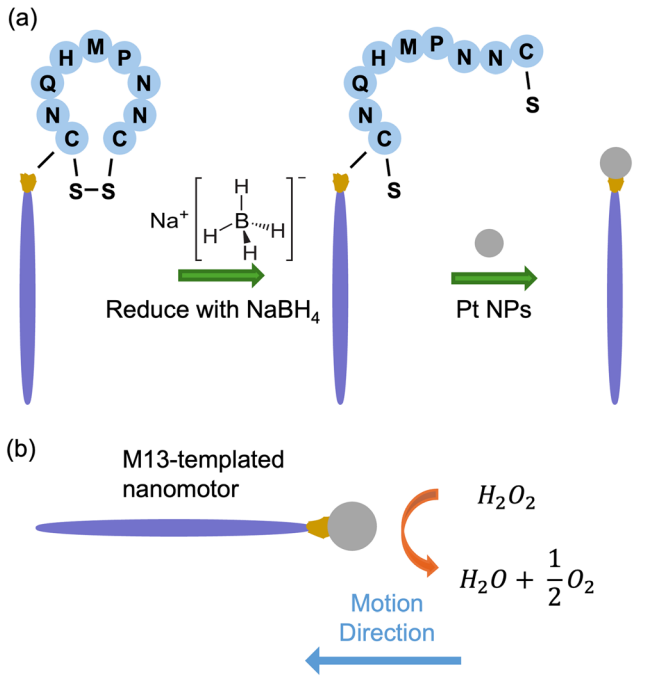


**Fig. 1** (a) Schematic of M13-templated nanomotor assembly approach. The M13 was fused with a peptide sequence (CNNPMHQNC) that brought two additional cysteines to each pIII minor coat protein. The cysteine residues on pIII were reduced using $NaBH_4$, breaking the disulfide bonds and generating free thiols. These thiols facilitated the binding of a Pt NP to the tip of M13 to form a Pt/M13 head/tail structure. (b) The catalytic self-propulsion of the M13-templated nanomotors is $H_2O_2$-driven.

## 2. Experimental details

### 2.1. Modification and amplification of M13 bacteriophage

For nanomotor assembly, a M13 bacteriophage was genetically modified to bind Pt nanoparticles using a previously reported protocol.[41,42] A cysteine-enriched peptide motif (CNNPMHQNC) was introduced into each of the five pIII minor coat proteins located at the proximal end of the phage.[43,44] This fusion increased the exposed cysteine residues within the pIII from six to eight, increasing the opportunity for metal–thiol interactions. Following modification, amplification and purification of the cysteine-enriched phage clone was conducted as previously described.[45] The M13 stock solution was suspended in 1× Tris-buffered saline (TBS, 50 mM Tris–HCl, 150 mM NaCl, pH 7.5) at a concentration of $1 \times 10^{11}$ pfu $\mu L^{-1}$ and stored at 4 °C.

### 2.2. Fabrication of Pt/M13 tadpole-shaped nanomotor

In order to ensure efficient metal–sulfur bonding between Pt nanoparticles and the M13 pIII minor coat protein, disulfide bonds within the viral capsid were reduced. A 100 μL volume of filamentous phage was diluted to a concentration of $1 \times 10^8$ pfu $\mu L^{-1}$ in 10 mM Tris–HCl. The reducing agent, sodium borohydride ($NaBH_4$, Sigma Aldrich), was prepared and mixed with the cysteine-enriched phage to reach a final concentration of 5 mM.[46] Reduction was performed in a 37 °C water bath for 30 min. Subsequently, the reducing agent was removed *via* diafiltration[47] (100 kDa MWCO Amicon® Ultra, MilliporeSigma). To minimize thiol re-oxidation, the deionized water used for diafiltration was pre-treated by bubbling $N_2$ through it for a minimum of 30 min and reduced phage were used immediately. The thiol concentration was measured using Ellman's reagent (DTNB, 5,5′-dithio-bis-(2-nitrobenzoic acid), Thermo Scientific) with a cysteine (L-cysteine hydrochloride monohydrate, Fisher BioReagents) standard curve, as shown in Fig. S1. For these experiments, after reduction and diafiltration, the phage solution was incubated with Ellman's reagent for 15 min and the absorbance at 412 nm was measured.

In preparation for nanomotor assembly, the as-received Pt nanoparticle solution (50 nm, $6.7 \times 10^{11}$ particles per mL, NanoComposix) was diluted with 2 mM sodium citrate to twice the molar concentration of phage. The diluted Pt nanoparticles and freshly reduced phage solutions were mixed in equal volumes and incubated at 37 °C for 6 h to allow binding. Subsequently, two differential centrifugal steps were completed to eliminate excess Pt nanoparticles, agglomerates, and unbound phage. First, the binding product was transferred to a microcentrifuge tube and spun at 500 rcf for 15 min. The supernatant, containing the nanomotors and free phage, was carefully collected and placed in a new microcentrifuge tube. Then, the collected liquid was centrifuged at 5000 rcf for 30 min. The upper liquid was discarded, and the pelleted Pt/M13 head/tail nanostructures were redispersed in deionized water for immediate use.

### 2.3. Characterization of nanomotor morphology and stability

Transmission electron microscopy (TEM, Talos L120C) was used to characterize nanomotor assembly and morphology. To prepare samples for imaging, formvar/carbon-coated copper grids (200 mesh, Ted Pella, Inc.) were glow discharged for 20 s using 20 mA of current. A volume of 5 μL nanomotor solution was added to each pre-treated grid, incubated for 5 min, and then rinsed twice with deionized water. Subsequently, samples were stained with 2% uranyl acetate for 30 s and wicked dry. For morphology evaluation, TEM images were captured in 40 randomly selected positions at a minimum magnification of 11 000×, such that at least 100 phages were observed per grid, and at least three grids were examined. ImageJ,[48] an open-source image program, was used to characterize and categorize the assembled structures.

To assess compatibility with fuel, bacteriophage was incubated in $H_2O_2$ at varying concentrations (0.2%–3%) and incubation times (up to 180 minutes), then titered. For each condition, 10 μL of serially diluted phage was added to 200 μL of ER2738 bacteria culture with an optical density of approximately 0.5 at 600 nm. The mixture was combined with agarose top, spread on agar plates, and incubated overnight at 37 °C. Plaque forming units (PFUs) were counted to determine phage concentration.

The Pt/M13 nanomotors were analyzed by dynamic light scattering (DLS) (Zetasizer Nano ZS90, Malvern Instruments, USA) and stability was assessed. Apparent size distribution measurements of nanomotors dispersed in deionized water were taken in triplicate at 0 h and after 3 h of incubation at 37 °C. For comparison, measurements were also taken of Pt nanoparticles under the same conditions.

### 2.4. Measurement of nanomotor motion

Confocal laser scanning microscopy (CLSM, Inverted Zeiss LSM880) was used to evaluate nanomotor motion. For these experiments, the cysteine-enriched M13 phage were dispersed in phosphate-buffered saline (PBS), tagged with an amine-reactive fluorescent dye (DyLight™ 550, ThermoScientific™), and redispersed in 1× Tris-buffered saline prior to nanomotor assembly. A glass bottom dish with lid and cover glass (Cellvis) was used for confocal imaging to minimize drift caused by solution evaporation or other environmental sources. The effect of a range of fuel concentrations (0%, 0.2%, 0.5%, 1%, 1.5% and 3% $H_2O_2$) was investigated. For each fuel condition, nanomotors were added to the fuel solution and their motion was recorded immediately. Movement was evaluated in six locations. Experiments were completed in at least triplicate. Videos were recorded using a 20× objective at a rate of 13 fps for up to 30 s. Using the TrackMate[49] plugin for Fiji,[50] nanomotor trajectories were acquired and analyzed from the video. A custom MATLAB code was employed to plot individual nanomotor trajectories and calculate, fit, and plot their mean square displacement (MSD), as well as to obtain nanomotor diffusion coefficients. Based on the definition, the MSD was calculated as:

$$\mathrm{MSD}(\Delta t) = \langle |\boldsymbol{x}(t_i + \Delta t) - \boldsymbol{x}(t_i)|^2 \rangle \quad (1)$$

where $\boldsymbol{x}(t_i)$ is the position vector of the nanomotor at time $t_i$.[51] For statistical robustness, only displacement in 1/4 of the maximum time interval of each track was used to plot and fit the MSD of the nanomotors.[52] The average and standard deviation of the MSD of all trajectories for each fuel concentration were calculated for comparison. The diffusion exponent and diffusion coefficient of the nanomotors were obtained by fitting the MSD as a function of time interval using the anomalous diffusion equation. This power law relationship is given as:[53,54]

$$\mathrm{MSD}(\Delta t) = 4D\Delta t^{\alpha} \quad (2)$$

where $\alpha$ is the diffusion exponent, $D$ is the diffusion coefficient, and $\Delta t$ is the time interval. The diffusion exponent was

 

obtained by taking the logarithm of both sides of the equation, then fitting $\alpha$ through a linear fit, as:[55]

$$\log(\mathrm{MSD}(\Delta t)) = \alpha \log(\Delta t) + \log(4D) \quad (3)$$

The steps in the first 0.4 s of selected time interval of each track were excluded during the linear fitting for diffusion exponent due to the noise at short times.[55] For comparison, the motion of dye-tagged cysteine-enriched M13 clones without attached Pt nanoparticles was recorded and analyzed using the same methods.

### 2.5. Nanomotor cell internalization

Cell internalization of nanomotors was evaluated *in vitro* using CLSM. Approximately $5 \times 10^4$ SKOV3 ovarian cancer cells (ATCC) per well were cultured in 100 μL of McCoy's 5A medium (30–2007, ATCC, Manassas, VA) supplemented with 10% fetal bovine serum (FBS) and 1% penicillin/streptomycin (Corning Inc., Corning, NY) in a 96-well plate at 37 °C with 5% $CO_2$. After seeding overnight, the culture medium was replaced with a mixture of 50 μL medium and 50 μL Dylight 550-tagged nanomotor solution containing either 0% $H_2O_2$ or 0.2% $H_2O_2$. The cells were incubated with nanomotors for 3 h, then washed three times with PBS and stained (LysoTracker™ Green DND-26, ThermoFisher) for 40 min. Cells were imaged immediately following staining. Photoexcitation wavelengths of 488 nm and 560 nm were used for Lysotracker and Dylight 550, respectively, while fluorescence emission was collected at 493–553 nm and 566–670 nm. Confocal microscopy images were falsely colored: Lysotracker emission (green channel), Dylight 550 emission (red channel), and bright field image (grey channel). A *z*-stack scanning was taken for each position with 1 μm interval and a total range of 70 μm. Three different positions from each well were scanned. Integrated fluorescence intensity was calculated for the nanomotor signal within a 50 μm range centered on the maximum lysosome fluorescence, ensuring signal was associated with internalized nanomotors. A total of twelve positions were randomly selected, analyzed and averaged for each condition. Pearson's *R* value was used to quantify the degree of correlation between nanomotor and lysosome fluorescence signals. The image processing software Fiji was used for both fluorescence intensity analysis and Pearson's *R* value calculation.

### 2.6. Evaluation of nanomotor photothermal properties

A continuous-wave (CW) NIR laser diode with a wavelength of 808 nm (LRD-0808-PFR02000-01; Laserglow Technologies, Toronto, ON, Canada) and spot size of 0.25 $cm^2$ was used to study the photothermal properties of the Pt/M13 nanomotors. A volume of 100 μL nanomotor (prepared by mixing 50 μL cell culture media with 50 μL of nanomotor solution, resulting in the same 100 μL mixture used in the internalization experiment) was placed in a polypropylene microcentrifuge tube with an approximate wall thickness of 0.7 mm for photothermal experiments. The microcentrifuge tube was placed in a tube rack with lid open. The nanomotor solution was irradiated from the top using the NIR laser. The power density of the laser was set at 1 W $cm^{-2}$, 2 W $cm^{-2}$, or 3 W $cm^{-2}$. The time for each photothermal irradiation treatment was 600 s. A thermal camera (C3, FLIR) was used to record the solution temperature from the side of the microcentrifuge tube during the NIR irradiation. The photothermal conversion efficiency of the system was calculated following a previously reported method as described in the SI.[56–60]

### 2.7. Cell viability assay

A live/dead staining (LIVE/DEAD™ Viability/Cytotoxicity Kit, for mammalian cells) was conducted to identify viable and dead cells. Culture media of cells after treatment with nanomotors or NIR irradiation was removed gently, and the cells were incubated with 100 μL of mixed dye solution containing Calcein AM (4 mM) and Ethidium homodimer-1 (2 mM). Staining was performed at room temperature for 30 min. Stained cells were imaged immediately with CLSM. Photoexcitation wavelengths of 488 nm and 561 nm were used for Calcein AM and Ethidium homodimer-1, respectively, while fluorescence emission was collected in the spectral ranges of 493–578 nm and 579–660 nm. Cell viability was determined used Fiji image analysis software. Using an 850 μm × 850 μm field of view, six locations were randomly selected, analyzed, and averaged to find the cell viability for each condition. For viability assays that included nanomotors, the cysteine-enriched M13 phage were tagged with an amine-reactive fluorescent dye (DyLight™ 650, ThermoScientific™) prior to assembly. For nanomotor imaging, a photoexcitation wavelength of 633 nm was used and fluorescence emission was collected from 659 to 759 nm.

## 3. Results and discussion

### 3.1. Fabrication and morphological characterization of Pt/M13 tadpole-shaped nanomotor

Five different structural proteins make-up the nearly one micron long M13 bacteriophage: two minor coat proteins at each end (proximal: pIII, pVI; distal: pIX, pVII) and one major coat protein along its length (pVIII). Whereas the pIII minor coat protein has six exposed cysteine residues, the pVIII major coat protein has none.[61] This nonuniform and orthogonal distribution of cysteine residues within the viral capsid presents an opportunity for assembly of tadpole-shaped Pt/M13 nanomotors. In these studies, to further increase template asymmetry, an additional peptide (CNNPMHQNC) was displayed near the N-terminus of each of the pIII minor coat proteins. This modification increased its exposed cysteine content by 33%. Following sodium borohydride reduction of the cysteine-enriched M13 clones, the free thiol groups were quantified with Ellman's reagent. On average, 82% of exposed cysteine residues were reduced. When mixed with 50 nm diameter Pt nanoparticles, these free thiols could facilitate the formation of metal–sulfur bonds with the tip of the virus causing low-symmetry Pt/M13 head/tail nanostructures to assemble.

The resulting M13-based nanostructures were studied with TEM. Representative images of the cysteine-enriched M13 clone and the assembled Pt/M13 nanomotors, both stained with uranyl acetate, are presented in Fig. 2. The cysteine-enriched M13 clones have a contour length of approximately 960 nm, as determined by TEM.[41] The Pt/M13 nanomotors exhibited the same filamentous structure and length with the addition of a single 50 nm Pt nanoparticle on one end. Following assembly and purification, 71% of the fabricated products were identified as Pt/M13 head/tail tadpole structures, while the remaining 29% consisted of structures that were more complex. As illustrated in Fig. S2, the complex structures can be divided into two main categories: those formed by interactions between (1) Pt nanoparticles and the pVIII major coat proteins, (2) Pt nanoparticles (or M13) and minor coat proteins at the M13 distal end. A similar range of morphologies has also been described for colloidal assembly of Au nanoparticles and M13 bacteriophage into head/tail and multi-armed structures.[62,63] These researchers observed that adjustment of M13 concentration and nanoparticle : M13 molar ratio affected structure formation. The Pt/M13 nanomotors were also analyzed with DLS. The resulting data are shown in Fig. S3 and S4. The observed multi-modal size distributions were a reflection of the high aspect ratio, semi-flexible M13 filament, as well as sample structural heterogeneity that encompassed both tadpoles and larger complex geometries. To assess stability, weighted averages (or *z*-averages) of the apparent size distribution were recorded at 0 and 3 h and are provided in Fig. S5. Some aggregation occurred within this time interval; however, the degree of colloidal stability was highly batch dependent. While additional work is necessary to increase head/tail particle assembly and decrease colloidal heterogeneity, the yield and stability achieved were sufficient for nanomotor motion measurement.

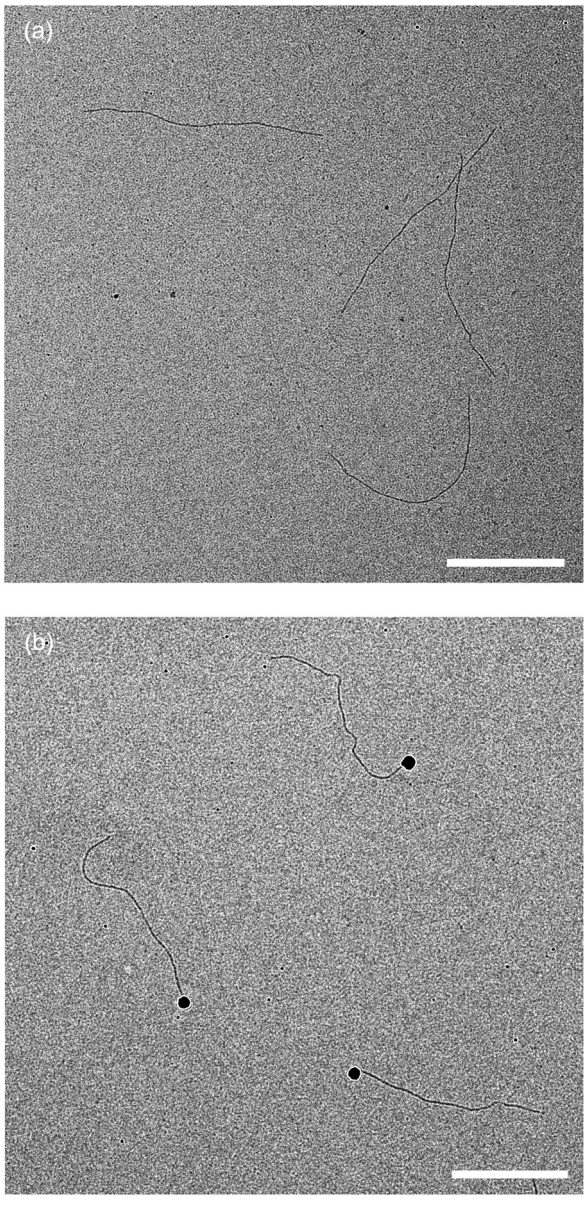


**Fig. 2** TEM images showing the morphologies of the (a) cysteine-enriched M13, as well as the (b) Pt/M13 nanomotor. Scale bar: 500 nm.

### 3.2. Analysis of nanomotor motion

Prior to motion analysis, plaque assays were used to confirm the compatibility of the M13 with $H_2O_2$ fuel. These measurements quantify infectivity, which often correlates with viral structural integrity. As shown in Fig. S6, exposure to $H_2O_2$ negatively affected phage infectivity. However, similar to a previous report that used 5% $H_2O_2$, effects were larger initially and declined over time revealing some percentage of phage remained infectious even with extended incubation.[64] Given an appropriate initial phage concentration, the residual phage were deemed sufficient to support the head/tail nanomotor structure within fuel.

M13-templated nanomotor motion was evaluated with CLSM. For these studies, the M13 was fluorescently tagged prior to nanomotor assembly. For reference, the absorbance spectra of the fluorescent dye, as well as the labeled and unlabeled M13 bacteriophage are plotted together in Fig. S7(a). The labeling was sufficient to clearly image the M13 virus (Fig. S7(b)). The motion of Pt/M13 nanomotors and M13 bacteriophage was recorded with CLSM in a range of fuel concentrations using a 20× objective at a rate of 13 fps for up to 30 s. Corresponding trajectories were acquired with the TrackMate plug-in. On average, an initial concentration between $10^7$ and $10^8$ pfu $\mu L^{-1}$ allowed visualization of approximately 2–3 nanomotors per 60 × 60 μm frame. The motion of Pt/M13 nanomotors in the absence and presence of $H_2O_2$ fuel is shown in Videos S1 and S2, respectively. Individual frames from these videos are also provided in Fig. S8 with overlaid trajectories. Using this approach, multiple motors could be simultaneously tracked and no drift was observed.

Typical tracked trajectories for Pt/M13 nanomotors in 0%, 0.2% and 3% $H_2O_2$ are depicted in Fig. 3(a)–(c). Trajectories for the other fuel concentrations are presented in Fig. S9. The trajectories display the increasing mobility of the nanomotors

 

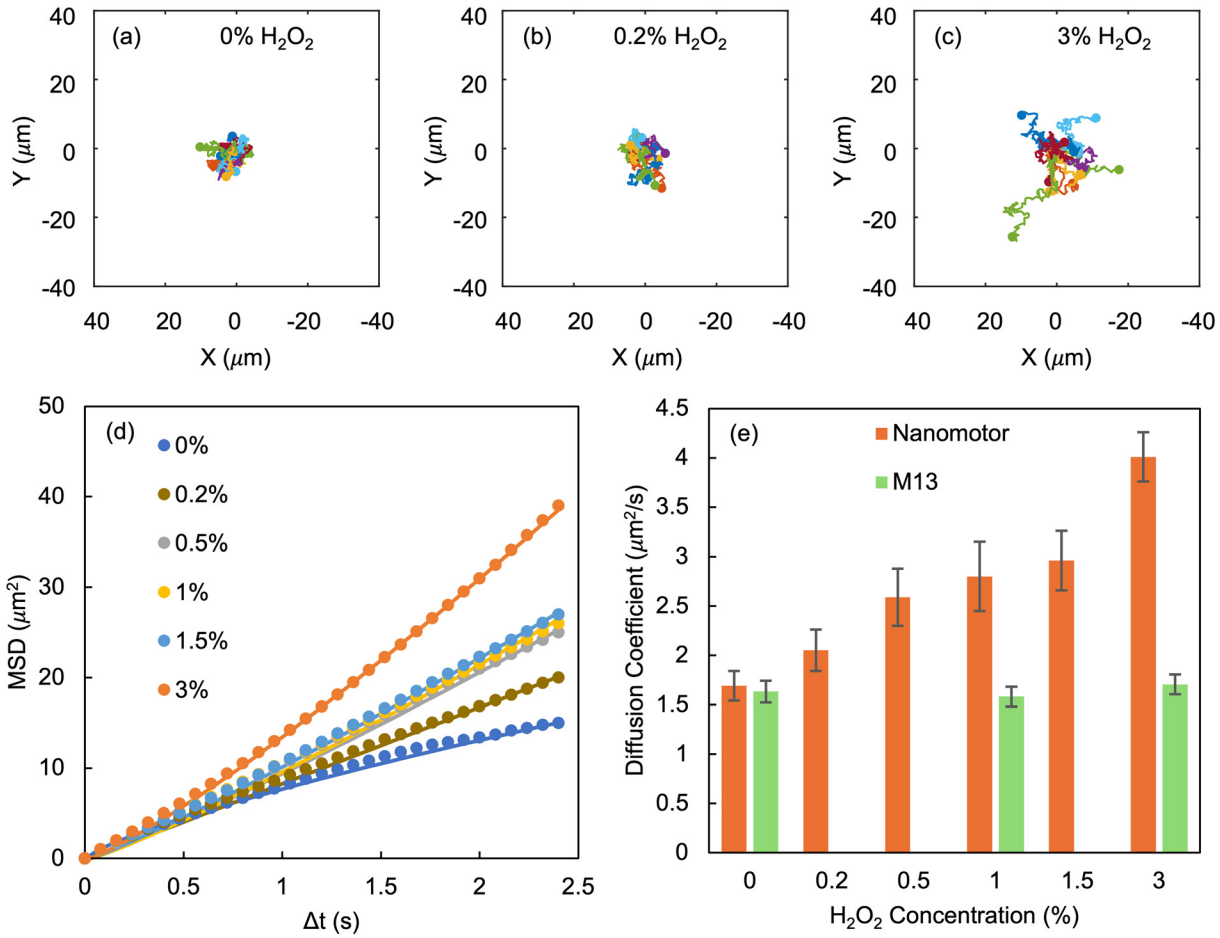


**Fig. 3** Motion analysis of viral-templated nanomotor. Trajectories of nanomotors in $H_2O_2$ concentrations of (a) 0%, (b) 0.2%, and (c) 3%. For each concentration, trajectories of 10 nanomotors were tracked over 120 frames and plotted together. Each trajectory is labeled with a distinct color and has been translated to the same origin. A circle has been placed at the end of each trajectory to show the direction of motion. (d) Average MSD data (circles) for Pt/M13 nanomotors depicted with fitted (lines) using the power law relationship of the anomalous diffusion equation. The scaling exponents in 0%, 0.2%, 0.5%, 1%, 1.5%, and 3% $H_2O_2$ were 0.88, 0.93, 0.96, 0.99, 1.05, and 1.18, respectively. (e) The diffusion coefficients, extracted from the fitted MSD curves, are shown for Pt/M13 nanomotors and M13.

with fuel concentration. A custom MATLAB code was employed to calculate the mean squared displacement (MSD) using coordinates extracted from recorded videos. Average MSD values are plotted as a function of time interval for each $H_2O_2$ concentration in Fig. 3(d). In addition, for completeness, individual MSD curves for nanomotors and M13 phage control experiments are provided in Fig. S10 and S11, respectively. An examination of individual MSD curves reveals a slightly larger MSD range for nanomotors than for phage. As mobility is likely reliant on Pt nanoparticle number and binding position, this difference could be associated with complex structures, aggregate formation, or degradation, among others. Further investigation is necessary to better understand the origins.

The power law relationship of the anomalous diffusion equation was used to estimate diffusion exponents and coefficients. Diffusion exponents of average nanomotor MSD curves ranged from 0.88 without fuel to 1.18 with 3% $H_2O_2$. These values are consistent with near linear, diffusive behavior.[65,66]

The estimated diffusion coefficients for Pt/M13 nanomotors, as well as M13 without Pt nanoparticles attached are found in Fig. 3(e) for a range of $H_2O_2$ fuel concentrations. The diffusion coefficients of the Pt/M13 nanomotor and M13 in 0% $H_2O_2$ were 1.69 ± 0.15 $\mu m^2\ s^{-1}$ and 1.63 ± 0.23 $\mu m^2\ s^{-1}$, respectively. These values are consistent with previous reports of M13 in aqueous solution measured with a variety of methods.[67–69] Without fuel, the addition of a Pt nanoparticle had little impact on bacteriophage motion. Notably, the effective diffusion coefficient of the nanomotors increased with $H_2O_2$ concentration, indicating fuel-dependent enhanced diffusion. With the addition of 0.2% and 3% $H_2O_2$, effective diffusion coefficients of 2.05 ± 0.21 $\mu m^2\ s^{-1}$ and 4.01 ± 0.25 $\mu m^2\ s^{-1}$ were extracted, respectively. These represent corresponding diffusion enhancements of 21% and 240% compared to Pt/M13 nanomotor motion in 0% $H_2O_2$. The lowest fuel concentration, 0.2% $H_2O_2$, was selected for subsequent *in vitro* investigations with tumorigenic cells.[70,71]

### 3.3. Quantification of nanomotor cell internalization

Cellular internalization of Pt/M13 nanomotors was studied using SKOV3 ovarian cancer cells. Although $H_2O_2$ is present at low concentrations within the human body (~0.1 μM) and is often overexpressed in tumor microenvironments (~50–100 μM), the extremely high concentrations of $H_2O_2$ used for Pt/M13 nanomotor fuel are generally incompatible with living cells.[72,73] For this reason, as shown in Fig. S12 and S13, the effect of $H_2O_2$ on SKOV3 cell viability was monitored using a live/dead cell assay prior to studying nanomotor cellular uptake. Optical and confocal fluorescence microscopy images of the cancer cells cultured in 0.2% $H_2O_2$ for 3 h with and without nanomotors are presented alongside images of cells

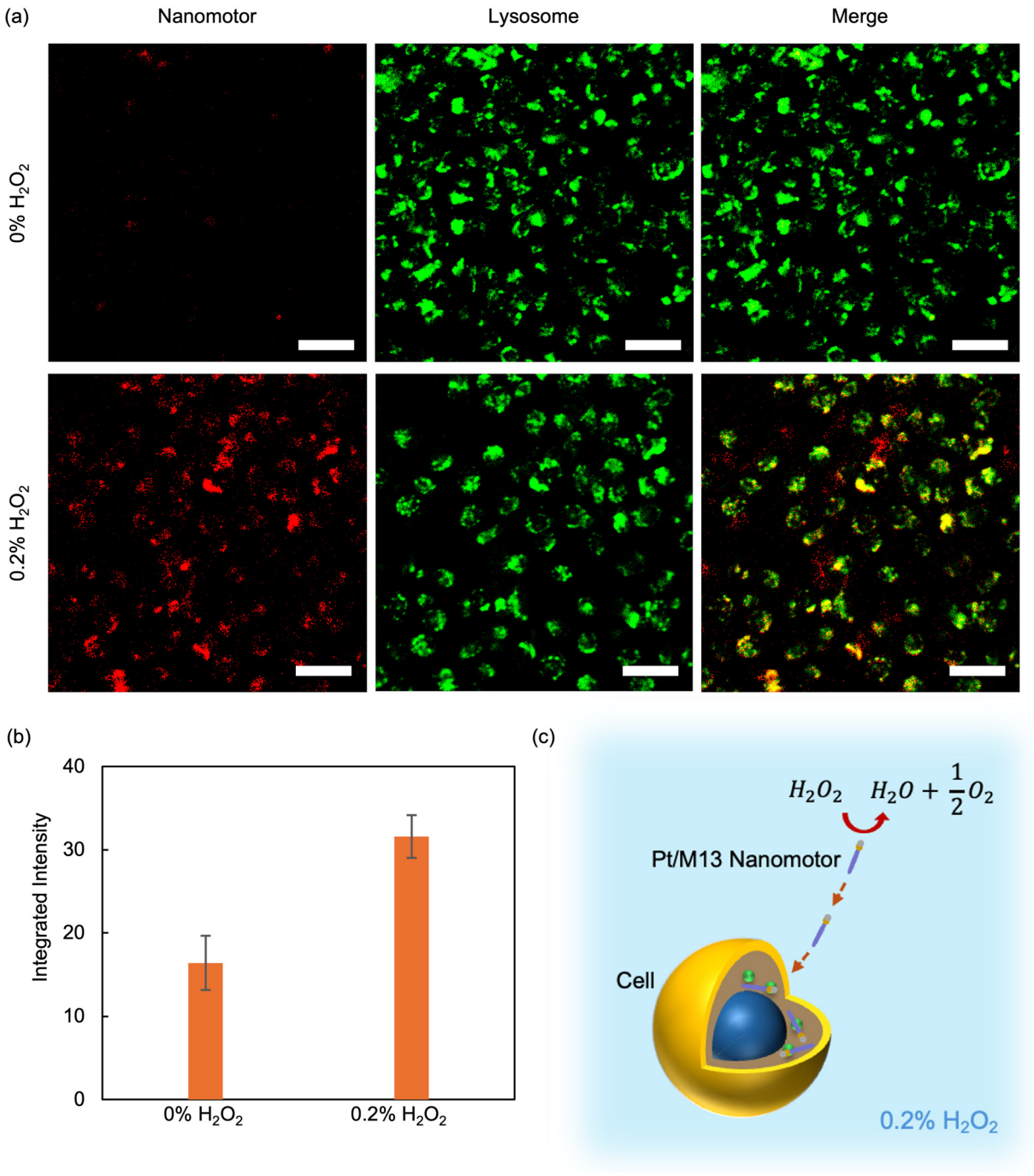


**Fig. 4** (a) Confocal fluorescence images of nanomotors (red), lysosomes (green), and merged signals in 0% and 0.2% $H_2O_2$. Scale bar: 100 μm. (b) Integrated fluorescence for internalized Pt/M13 nanomotors following incubation with 0% and 0.2% $H_2O_2$. (c) Schematic of Pt/M13 nanomotor $H_2O_2$ fuel-driven motion and enhanced SKOV3 cell uptake.

prepared without $H_2O_2$, as a control. Live cells stained with Calcein AM appear green and dead cells stained with Ethidium homodimer-1 appear red. When incubated with $H_2O_2$ alone, the cell density decreased considerably and the few remaining cells displayed only 6.7% viability, thus demonstrating the toxicity of 0.2% $H_2O_2$ to the cells. Interestingly, when both nanomotors and $H_2O_2$ were introduced simultaneously, cell density was preserved and 97% viability was achieved. Based on previous reports of both $H_2O_2$-driven nanomotors and Pt nanoparticle antioxidant properties,[74–77] we speculate that Pt-induced catalytic degradation locally decreased the $H_2O_2$ concentration, reducing $H_2O_2$-related oxidative cell damage. Additional studies are necessary to elucidate the mechanism more fully.

The uptake of Pt/M13 nanomotors by SKOV3 cells was investigated with CLSM in the presence and absence of 0.2% $H_2O_2$ fuel for 3 h. Confocal fluorescence microscopy images of cellular internalization are shown in Fig. 4(a). For visualization, nanomotors were labeled with Dylight 550 (red), while lysosomes were stained with Lysotracker (green). In the absence of $H_2O_2$, only weak red fluorescence was observed, suggesting limited nanomotor internalization. In contrast, strong red emission was seen with added 0.2% $H_2O_2$, indicating significantly enhanced nanomotor uptake. Merged nanomotor and lysosome fluorescence images corroborated the intracellular observation plane and further verified internalization.

Analysis of consecutive confocal fluorescence sections using 1 μm scan intervals established the presence of nanomotors throughout the cells. The integrated intensity of *z*-stack fluorescence with and without fuel is plotted in Fig. 4(b). Cellular nanomotor uptake was nearly doubled with the addition of 0.2% $H_2O_2$. As illustrated in Fig. 4(c), Pt/M13 nanomotors were propelled by $H_2O_2$, enhancing diffusion and, ultimately, considerably increasing uptake by SKOV3 cells. Both internalization and intracellular distribution contribute to nanomotor effectiveness as a therapeutic, therefore the spatial overlap between the nanomotor and lysosome fluorescence was quantified using Pearson's correlation coefficient (R).[37,78] In this colocalization analysis, an *R* value of 1 represents complete correlation, whereas a value of 0 signifies no correlation. The calculation generated an *R* value of 0.74, indicating strong colocalization of nanomotors and lysosomes after 3 h of $H_2O_2$ fuel exposure.[79,80] Interestingly, this observation is consistent with a previous report of untargeted or nonspecific M13 bacteriophage uptake.[81] In these studies, virus internalization was examined over a span of 24 h for a variety of endothelial and epithelial cells (*e.g.* HeLa, MCF-7, HDMEC). The comparable outcomes suggest that the addition of the Pt nanoparticle for nanomotor formation does not preclude cellular uptake nor its accumulation in lysosomes; however, additional studies are needed to fully understand the endocytic pathway of the head/tail structures along with the role of complex structures in cell uptake. Others have demonstrated that the addition of specific targeting peptides to the M13 viral capsid can substantially alter its fate, causing it to be collected in certain organelles or even the cytosol following internalization.[12,82] Future experiments will seek to better understand the effect of targeting peptides in M13-based nanomotor cellular uptake and intracellular distribution.

### 3.4. Photothermal performance of Pt/M13 nanomotor

A continuous wave 808 nm laser was used to study the photothermal properties of Pt/M13 nanomotors. The optical absorbance spectrum of the nanomotors is shown in Fig. S14 at a concentration of $2 \times 10^7$ nanomotor per μL. A thermal camera was used to measure temperature changes under NIR illumination for a range of power densities. As depicted in Fig. 5(a), under all irradiation conditions (1 W $cm^{-2}$, 2 W $cm^{-2}$, 3 W $cm^{-2}$), nanomotor solution temperatures increased within a 600 s exposure time. Perhaps not surprisingly, the largest temperature rise was observed for the highest power density investigated. Using 3 W $cm^{-2}$ irradiation, nanomotors experienced a temperature rise of approximately 25 °C, which can

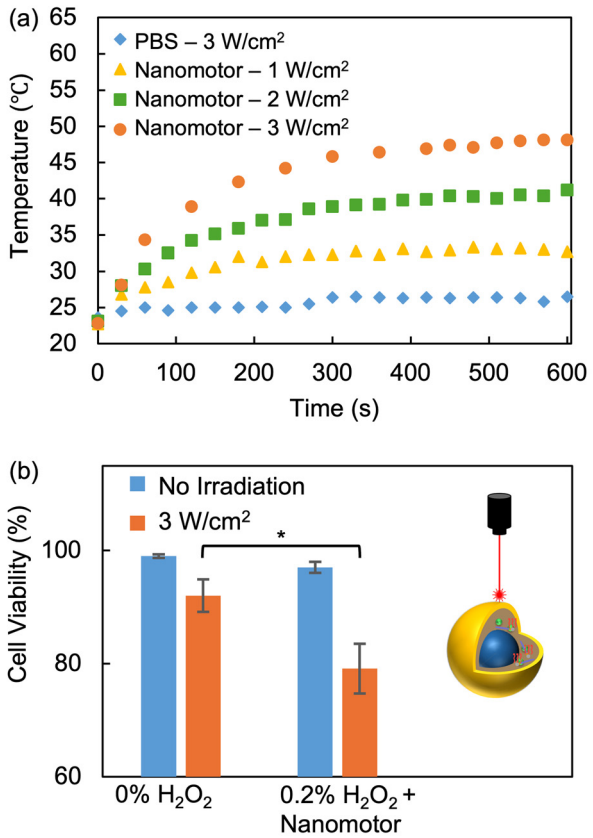


**Fig. 5** (a) The temperature of nanomotor solution plotted against irradiation time with power densities ranging from 1 W $cm^{-2}$ to 3 W $cm^{-2}$. The temperature increase of PBS under 3 W $cm^{-2}$ irradiation was also measured as a control. (b) Quantified cell viability of SKOV3 cells treated with Pt/M13 nanomotors and 0.2% $H_2O_2$, without and with 3 W $cm^{-2}$ NIR irradiation. For comparison, the viability of untreated cells was also measured. Inset: schematic of SKOV3 cells with internalized nanomotors irradiated with 808 nm laser. The NIR light was absorbed and converted to heat, triggering photothermal injury to cell.

further be increased by increasing the power density to induce irreversible cell damage.[83,84] In contrast, under the same conditions, the buffer temperature only increased by 3 °C. The calculated photothermal conversion efficiency, $\eta$, of the Pt/M13 nanomotors was 32.6% (Fig. S15).

Based on this performance, the *in vitro* photothermal effects of the Pt/M13 nanomotors on SKVO3 cells were evaluated. After co-incubation with nanomotors and 0.2% $H_2O_2$ for 3 h, SKOV3 cells were subjected to 3 W $cm^{-2}$ of NIR laser light for 600 s. As shown in Fig. 5(b) and S16, a live/dead assay was used to visualize and quantify the viability of the cells with and without 808 nm irradiation. Without NIR treatment, the overwhelming majority, or approximately 97%, of the cells emitted green fluorescence, signaling that co-incubation had minimal effect on the viability of the cells. With 808 nm laser irradiation, a notable uptick in red emitting or dead cells was observed and cell survival was lowered to 79%. As NIR light is absorbed and converted to heat, the temperature of the nanomotor and its proximity rise. The observed reduction in cell viability, while less than anticipated, clearly demonstrated the Pt/M13 nanomotor potential for photothermal therapy. Future studies will aim to increase cellular uptake through the addition of targeting peptides and/or the use of higher nanomotor concentrations, as well as optimize laser irradiation parameters.

## 4. Conclusion

In this work, we created a tadpole-shaped nanomotor using the filamentous M13 bacteriophage, a highly effective viral nanocarrier, as a template. Its head/tail geometry was formed by simply adding a Pt nanoparticle to one tip. In the presence of $H_2O_2$ fuel, this minor modification transformed the motion of the virus from passive diffusion to active propulsion. CLSM was used to record the trajectories of dye-tagged Pt/M13 nanomotors in a range of $H_2O_2$ concentrations. MSD analysis correlated higher fuel concentrations with greater mobility. Compared to M13 phage, the tadpole-like nanomotors experienced considerably enhanced diffusion. Their improved transport significantly boosted internalization by SVOK3 ovarian cancer cells *in vitro*, allowing evaluation of Pt/M13 nanomotor photothermal effects on cell viability using NIR illumination. By leveraging the characteristic asymmetry of the M13 phage capsid, we have demonstrated the straightforward conversion of the filamentous virus to a simple fuel-driven nanomotor. While the reported device was powered by $H_2O_2$ concentrations too high to be biologically relevant, the adaptability of the M13 coat proteins is already well established. In future incarnations, the surface chemistry of the viral scaffold can be readily engineered to bind nanozymes more favorable to propulsion *via* less toxic fuels (*e.g.* urea, glucose) or externally applied fields (*e.g.* electromagnetic, thermal). Likewise, affinity fusions and large payloads can be incorporated within the capsid to expand targeting and cargo delivery capacity, as already demonstrated by M13 nanocarriers.[7–15] The integration of the M13 bacteriophage, a proven viral nanocarrier, with nanomotor active diffusion reveals the potential for faster, non-invasive delivery of M13-based therapeutics, diagnostics, and imaging agents in the future, with a view to advancing precision nanomedicine.

## Conflicts of interest

There are no conflicts of interest to declare.

## Data availability

The data supporting this article have been included as part of the supplementary information (SI). Supplementary information is available. See DOI: **https://doi.org/10.1039/d5nr02501j**.

## Acknowledgements

This material is based upon research supported by the National Science Foundation under Award No. 2002941. In addition, this study made use of the TEM Talos120C in the Central Facility for Advanced Microscopy and Microanalysis (CFAMM) and the Zeiss LSM 880 inverted confocal microscope in the Microscopy and Imaging Core Facility (Core), as well as the Genomics Core Facility at UC Riverside.

## References

1 C. Zhang, L. Yan, X. Wang, S. Zhu, C. Chen, Z. Gu and Y. Zhao, *Nano Today*, 2020, **35**, 101008.
2 E. D. Namiot, A. V. Sokolov, V. N. Chubarev, V. V. Tarasov and H. B. Schiöth, *Int. J. Mol. Sci.*, 2023, **24**, 787.
3 X.-T. Li, S.-Y. Peng, S.-M. Feng, T.-Y. Bao, S.-Z. Li and S.-Y. Li, *Small*, 2024, **20**, 2307111.
4 Y. H. Chung, H. Cai and N. F. Steinmetz, *Adv. Drug Delivery Rev.*, 2020, **156**, 214–235.
5 B. Ikwuagwu and D. Tullman-Ercek, *Curr. Opin. Biotechnol.*, 2022, **78**, 102785.
6 S. Zanganeh, M. Doroudian, Z. R. Nowzari, P. Nasirmoghadas, J. S. Nahand, S. Sepehrpour and M. Moghoofei, *Adv. Ther.*, 2023, **6**, 2300082.
7 C. Chang, W. Guo, X. Yu, C. Guo, N. Zhou, X. Guo, R.-L. Huang, Q. Li and Y. Zhu, *Mater. Today Bio*, 2023, **20**, 100612.
8 D. Ghosh, A. F. Bagley, Y. J. Na, M. J. Birrer, S. N. Bhatia and A. M. Belcher, *Proc. Natl. Acad. Sci. U. S. A.*, 2014, **111**, 13948–13953.
9 L. Ceppi, N. M. Bardhan, Y. Na, A. Siegel, N. Rajan, R. Fruscio, M. G. Del Carmen, A. M. Belcher and M. J. Birrer, *ACS Nano*, 2019, **13**, 5356–5365.
10 T. Yang, Q. Zhang, Y. Miao, Y. Lyu, Y. Xu, M. Yang and C. Mao, *Adv. Mater.*, 2025, **37**, 2403756.

 

11 E. Turrini, L. Ulfo, P. E. Costantini, R. Saporetti, M. Di Giosia, M. Nigro, A. Petrosino, L. Pappagallo, A. Kaltenbrunner, A. Cantelli, V. Pellicioni, E. Catanzaro, C. Fimognari, M. Calvaresi and A. Danielli, *Cell. Mol. Life Sci.*, 2024, **81**, 144.
12 B. Bortot, M. Apollonio, G. Baj, L. Andolfi, L. Zupin, S. Crovella, M. di Giosia, A. Cantelli, R. Saporetti, L. Ulfo, A. Petrosino, G. Di Lorenzo, F. Romano, G. Ricci, M. Mongiat, A. Danielli, M. Calvaresi and S. Biffi, *Free Radicals Biol. Med.*, 2022, **179**, 242–251.
13 U. Tsedev, C.-W. Lin, G. T. Hess, J. N. Sarkaria, F. C. Lam and A. M. Belcher, *ACS Nano*, 2022, **16**, 11676–11691.
14 P. E. Costantini, R. Saporetti, M. Iencharelli, S. Flammini, M. Montrone, G. Sanità, V. De Felice, E. J. Mattioli, M. Zangoli, L. Ulfo, M. Nigro, T. Rossi, M. Di Giosia, E. Esposito, F. Di Maria, A. Tino, C. Tortiglione, A. Danielli and M. Calvaresi, *Small*, 2025, **21**, 2405832.
15 X. Dong, P. Pan, D.-W. Zheng, P. Bao, X. Zeng and X.-Z. Zhang, *Sci. Adv.*, 2020, **6**, eaba1590.
16 T. T. Ngo-Duc, Z. Alibay, J. M. Plank, J. E. Cheeney and E. D. Haberer, *ACS Appl. Mater. Interfaces*, 2020, **12**, 126–134.
17 H. Peng, D. Rossetto, S. S. Mansy, M. C. Jordan, K. P. Roos and I. A. Chen, *ACS Nano*, 2022, **16**, 4756–4774.
18 C.-Y. Kao, Y.-C. Pan, Y.-H. Hsiao, S.-K. Lim, T.-W. Cheng, S.-W. Huang, S. M.-Y. Wu, C.-P. Sun, M.-H. Tao and K. Y. Mou, *ACS Nano*, 2023, **17**, 14532–14544.
19 D. Frenkel and B. Solomon, *Proc. Natl. Acad. Sci. U. S. A.*, 2002, **99**, 5675–5679.
20 A. Ksendzovsky, S. Walbridge, R. C. Saunders, A. R. Asthagiri, J. D. Heiss and R. R. Lonser, *J. Neurosurg.*, 2012, **117**, 197–203.
21 L. Ulfo, A. Cantelli, A. Petrosino, P. E. Costantini, M. Nigro, F. Starinieri, E. Turrini, S. K. Zadran, G. Zuccheri, R. Saporetti, M. D. Giosia, A. Danielli and M. Calvaresi, *Nanoscale*, 2022, **14**, 632–641.
22 S. D. Branston, E. C. Stanley, J. M. Ward and E. Keshavarz-Moore, *Biotechnol. Bioprocess Eng.*, 2013, **18**, 560–566.
23 J. R. Brigati and V. A. Petrenko, *Anal. Bioanal. Chem.*, 2005, **382**, 1346–1350.
24 C. M. Warner, N. Barker, S.-W. Lee and E. J. Perkins, *Bioprocess Biosyst. Eng.*, 2014, **37**, 2067–2072.
25 P. Passaretti, I. Khan, T. R. Dafforn and P. Goldberg Oppenheimer, *Sci. Rep.*, 2020, **10**, 18538.
26 J. Yong, A. S. Mellick, J. Whitelock, J. Wang and K. Liang, *Adv. Mater.*, 2023, **35**, 2205746.
27 G. Rucinskaite, S. A. Thompson, S. Paterson and R. De La Rica, *Nanoscale*, 2017, **9**, 5404–5407.
28 D. Fang, T. Li, Z. Wu, Q. Wang, M. Wan, M. Zhou and C. Mao, *J. Mater. Chem. B*, 2021, **9**, 8659–8666.
29 A. C. Hortelão, R. Carrascosa, N. Murillo-Cremaes, T. Patiño and S. Sánchez, *ACS Nano*, 2019, **13**, 429–439.
30 S. S. Andhari, R. D. Wavhale, K. D. Dhobale, B. V. Tawade, G. P. Chate, Y. N. Patil, J. J. Khandare and S. S. Banerjee, *Sci. Rep.*, 2020, **10**, 4703.
31 S. Tang, F. Zhang, H. Gong, F. Wei, J. Zhuang, E. Karshalev, B. Esteban-Fernández de Ávila, C. Huang, Z. Zhou, Z. Li, L. Yin, H. Dong, R. H. Fang, X. Zhang, L. Zhang and J. Wang, *Sci. Robot.*, 2020, **5**, eaba6137.
32 N. Ruiz-González, D. Esporrín-Ubieto, I.-D. Kim, J. Wang and S. Sánchez, *ACS Nano*, 2025, **19**, 8411–8432.
33 H. Cheng, B. Ma, A. Ji, H. Yao, P. Chen, W. Zhai, S. Gao, L. Shi and H. Hu, *Biomater. Res.*, 2025, **29**, 0155.
34 M. M. Wan, H. Chen, Z. Da Wang, Z. Y. Liu, Y. Q. Yu, L. Li, Z. Y. Miao, X. W. Wang, Q. Wang, C. Mao, J. Shen and J. Wei, *Adv. Sci.*, 2021, **8**, 2002525.
35 J. Ren, Z. Chen, E. Ma, W. Wang, S. Zheng and H. Wang, *Colloids Surf., B*, 2023, **231**, 113568.
36 W. Cao, W. Wei, B. Qiu, Y. Liu, S. Xie, Q. Fang and X. Li, *Chem. Eng. J.*, 2024, **483**, 149187.
37 H. Chen, T. Li, Z. Liu, S. Tang, J. Tong, Y. Tao, Z. Zhao, N. Li, C. Mao, J. Shen and M. Wan, *Nat. Commun.*, 2023, **14**, 941.
38 X. Ma, K. Hahn and S. Sanchez, *J. Am. Chem. Soc.*, 2015, **137**, 4976–4979.
39 Z. Zhang, D. Zhang, B. Qiu, W. Cao, Y. Liu, Q. Liu and X. Li, *Nanoscale*, 2021, **13**, 6545–6557.
40 J. A. Tejeda-Rodríguez, A. Núñez, F. Soto, V. García-Gradilla, R. Cadena-Nava, J. Wang and R. Vazquez-Duhalt, *ChemNanoMat*, 2019, **5**, 194–200.
41 J. M. Plank, Z. Alibay, T.-T. Ngo-Duc, M. Lai, E. A. S. Mayes and E. D. Haberer, *ACS Appl. Nano Mater.*, 2020, **3**, 10668–10677.
42 V. A. Petrenko and G. P. Smith, *Protein Eng.*, 2000, **13**, 589–592.
43 Y. Huang, C. Y. Chiang, S. K. Lee, Y. Gao, E. L. Hu, J. De Yoreo and A. M. Belcher, *Nano Lett.*, 2005, **5**, 1429–1434.
44 S.-W. Lee, C. Mao, C. E. Flynn and A. M. Belcher, *Science*, 2002, **296**, 892–895.
45 J. M. Plank, Z. Alibay, T. T. Ngo-Duc, M. Lai, E. A. S. Mayes and E. D. Haberer, Bifunctional M13 Bacteriophage Nanospheroids for the Synthesis of Hybrid Noncentrosymmetric Nanoparticles, *ACS Appl. Nano Mater.*, 2020, **3**(11), 10668.
46 J. M. Plank, PhD thesis, University of California, Riverside, 2019.
47 L. Schwartz, *BioProcess Int.*, 2003, **1**, 43–49.
48 C. A. Schneider, W. S. Rasband and K. W. Eliceiri, *Nat. Methods*, 2012, **9**, 671–675.
49 D. Ershov, M.-S. Phan, J. W. Pylvänäinen, S. U. Rigaud, L. Le Blanc, A. Charles-Orszag, J. R. W. Conway, R. F. Laine, N. H. Roy, D. Bonazzi, G. Duménil, G. Jacquemet and J.-Y. Tinevez, *Nat. Methods*, 2022, **19**, 829–832.
50 J. Schindelin, I. Arganda-Carreras, E. Frise, V. Kaynig, M. Longair, T. Pietzsch, S. Preibisch, C. Rueden, S. Saalfeld, B. Schmid, J.-Y. Tinevez, D. J. White, V. Hartenstein, K. Eliceiri, P. Tomancak and A. Cardona, *Nat. Methods*, 2012, **9**, 676–682.
51 C. Bechinger, R. Di Leonardo, H. Löwen, C. Reichhardt, G. Volpe and G. Volpe, *Rev. Mod. Phys.*, 2016, **88**, 045006.

52 W. Wang and T. E. Mallouk, *ACS Nano*, 2021, **15**, 15446–15460.
53 M. S. Draz, K. M. Kochehbyoki, A. Vasan, D. Battalapalli, A. Sreeram, M. K. Kanakasabapathy, S. Kallakuri, A. Tsibris, D. R. Kuritzkes and H. Shafiee, *Nat. Commun.*, 2018, **9**, 4282.
54 Z. Lyu, L. Yao, Z. Wang, C. Qian, Z. Wang, J. Li, C. Liu, Y. Wang and Q. Chen, *ACS Nano*, 2024, **18**, 14231–14243.
55 D. S. Martin, M. B. Forstner and J. A. Käs, *Biophys. J.*, 2002, **83**, 2109–2117.
56 X. Cui, Q. Ruan, X. Zhuo, X. Xia, J. Hu, R. Fu, Y. Li, J. Wang and H. Xu, *Chem. Rev.*, 2023, **123**, 6891–6952.
57 Q. Wang, H. Wang, Y. Yang, L. Jin, Y. Liu, Y. Wang, X. Yan, J. Xu, R. Gao, P. Lei, J. Zhu, Y. Wang, S. Song and H. Zhang, *Adv. Mater.*, 2019, **31**, 1904836.
58 Z. Yan, N. Ding, S. Lin, S. Zhang, Y. Xiao, Y. Xie and S. Zhang, *Biomacromolecules*, 2024, **25**, 6840–6854.
59 B. Ma, Y. Yu, J. Li, Y. Zhang, B. Sun, A. Ji, K. Song, L. Shi, H. Hu, S. Gao and H. Cheng, *Small*, 2024, **20**, 2403800.
60 M. Manikandan, N. Hasan and H.-F. Wu, *Biomaterials*, 2013, **34**, 5833–5842.
61 D. Montalvan-Sorrosa, J. L. González-Solis, J. Mas-Oliva and R. Castillo, *RSC Adv.*, 2014, **4**, 57329–57336.
62 H. Ahmed, H. Lopez, F. Boselli, G. Tarricone, S. Vercellino, P. E. Costantini, V. Castagnola, M. Veronesi, F. Benfenati, A. Danielli, L. Boselli and P. P. Pompa, *ACS Nano*, 2024, **18**, 21302–21315.
63 A. De La Cotte, C. Wu, M. Trévisan, A. Repula and E. Grelet, *ACS Nano*, 2017, **11**, 10616–10622.
64 L. M. D. Plano, D. Franco, M. G. Rizzo, V. Zammuto, C. Gugliandolo, L. Silipigni, L. Torrisi and S. P. P. Guglielmino, *Int. J. Mol. Sci.*, 2021, **22**, 3408.
65 I. N. Unksov, C. S. Korosec, P. Surendiran, D. Verardo, R. Lyttleton, N. R. Forde and H. Linke, *ACS Nanosci. Au*, 2022, **2**, 140–159.
66 M. J. Saxton and K. Jacobson, *Annu. Rev. Biophys. Biomol. Struct.*, 1997, **26**, 373–399.
67 J. Newman, H. L. Swinney and L. A. Day, *J. Mol. Biol.*, 1977, **116**, 593–603.
68 M. Smith, R. Poling-Skutvik, A. H. Slim, R. C. Willson and J. C. Conrad, *Macromolecules*, 2021, **54**, 4557–4563.
69 K. Beck and R. M. Duenk, *J. Struct. Biol.*, 1990, **105**, 22–27.
70 A. Llopis-Lorente, A. García-Fernández, E. Lucena-Sánchez, P. Díez, F. Sancenón, R. Villalonga, D. A. Wilson and R. Martínez-Máñez, *Chem. Commun.*, 2019, **55**, 13164–13167.
71 M. Xuan, J. Shao, X. Lin, L. Dai and Q. He, *ChemPhysChem*, 2014, **15**, 2255–2260.
72 J. Li, Z. Wei, X. Lin, D. Zheng, M. Wu, X. Liu and J. Liu, *Adv. Healthcare Mater.*, 2019, **8**, 1801627.
73 Z. Chu, J. Yang, W. Zheng, J. Sun, W. Wang and H. Qian, *Coord. Chem. Rev.*, 2023, **481**, 215049.
74 J.-W. Lee, J. Son, K.-M. Yoo, Y. M. Lo and B. Moon, *RSC Adv.*, 2014, **4**, 19824.
75 A. Clark, A. Zhu, K. Sun and H. R. Petty, *J. Nanopart. Res.*, 2011, **13**, 5547–5555.
76 D. Pedone, M. Moglianetti, E. De Luca, G. Bardi and P. P. Pompa, *Chem. Soc. Rev.*, 2017, **46**, 4951–4975.
77 J. Sun, M. Mathesh, W. Li and D. A. Wilson, *ACS Nano*, 2019, **13**, 10191–10200.
78 J. M. Burns, R. Vankayala, J. T. Mac and B. Anvari, *ACS Appl. Mater. Interfaces*, 2018, **10**, 27621–27630.
79 K. W. Dunn, M. M. Kamocka and J. H. McDonald, *Am. J. Physiol.: Cell Physiol.*, 2011, **300**, C723–C742.
80 A. P. French, S. Mills, R. Swarup, M. J. Bennett and T. P. Pridmore, *Nat. Protoc.*, 2008, **3**, 619–628.
81 Y. Tian, M. Wu, X. Liu, Z. Liu, Q. Zhou, Z. Niu and Y. Huang, *Adv. Healthcare Mater.*, 2015, **4**, 413–419.
82 A. Kim, T.-H. Shin, S.-M. Shin, C. D. Pham, D.-K. Choi, M.-H. Kwon and Y.-S. Kim, *PLoS One*, 2012, **7**, e51813.
83 D. Jaque, L. M. Maestro, B. del Rosal, P. Haro-Gonzalez, A. Benayas, J. L. Plaza, E. M. Rodríguez and J. G. Solé, *Nanoscale*, 2014, **6**, 9494–9530.
84 M. Overchuk, R. A. Weersink, B. C. Wilson and G. Zheng, *ACS Nano*, 2023, **17**, 7979–8003.